The Astrophysical Journal, 934:127 (5pp), 2022 August 1 https://doi.org/10.3847/1538-4357/ac7b85

Target and Velocity Dependence of Charge Exchange X-Ray Emission at Solar Wind Velocities

R. T. Zhang[1,2], D. G. Seely[3,7], V. M. Andrianarijaona[4], F. Jaeckel[5], D. Wulf[5], K. Morgan[5], D. McCammon[5], and C. C. Havener[6]
[1] Institute of Modern Physics, Chinese Academy of Sciences, Lanzhou 730000, People's Republic of China; zhangrt@impcas.ac.cn
[2] University of Chinese Academy of Sciences, Beijing 100049, People's Republic of China
[3] Department of Physics, Albion College, Albion, MI 49224, USA
[4] Department of Physics and Engineering, Southern Adventist University, Collegedale, TN 37315, USA
[5] Department of Physics, University of Wisconsin, Madison, WI 53706, USA
[6] Physics Division, Oak Ridge National Laboratory, Oak Ridge, TN 37831-6368, USA
Received 2022 May 18; revised 2022 June 21; accepted 2022 June 21; published 2022 August 1

Abstract

Laboratory measurements of X-ray emissions following charge exchange (CX) between highly charged ions and neutrals are important to assess their diagnostic utility for the nonequilibrium astrophysical plasma environments, where hot flows meet cold gases. With a high-resolution X-ray quantum microcalorimeter detector, we report the CX-induced X-ray spectra and line ratios in Ne^{8+} on He and Kr collisions at solar wind velocities of 392, 554, 678, and 876 km s^{-1}, respectively. The experimentally determined line ratios quantify the differences in CX state selectivity and the following X-ray emission between He and Kr at different collision velocities. This suggests that target and velocity dependence should be considered for accurately modeling astrophysical CX plasmas.

Unified Astronomy Thesaurus concepts: Atomic spectroscopy (2099); Atomic physics (2063); Collision processes (2065); Atomic data benchmarking (2064); Charge exchange recombination (2062)

1. Introduction

Since the first observation of X-ray emission from Comet C/Hyakutake (Lisse et al. 1996) and explanation based on solar wind ions charge exchange (CX; Cravens 1997), many CX X-ray sources have been found when solar wind ions pass through heliospheric, geocorona, planetary atmosphere (Cravens 1997, 2000; Holmström et al. 2001; Cravens 2002; Beiersdorfer et al. 2003; Lallement 2004; Robertson et al. 2009), etc. Recently, CX is also considered as a promising mechanism for astrophysical CX plasmas such as supernova remnants (Katsuda et al. 2011; Cumbee et al. 2014), star-forming regions in nearby galaxies (Liu et al. 2012), extragalactic flows (Fabian et al. 2011), etc.

Modeling the observed X-ray spectra allows one to derive information such as composition, density, and relative velocities as well as ionization balance of the astrophysical CX plasma (Kuntz 2018). This has turned out to be significantly determined by principal n and orbital angular momentum l-resolved state-selective CX cross sections (Smith et al. 2014). Generally, these cross-section data are obtained through collecting reported results or semiclassical calculations. For instance, Bodewits et al. (2007) compiled the theoretical n, l state-selective CX cross sections from atomic and molecular orbital close coupling calculations, and concluded that 0.3–1 keV cometary X-ray emissions mainly result from CX between fully stripped and H-like C, N, O, Ne, etc. ions and H_2O and its dissociation products. Mullen et al. (2017) theoretically modeled solar wind X-ray data from Comet C/2000 WM1 using the results from a multichannel Landau–Zener (MCLZ) method, and concluded that the X-ray intensity is dominated by solar wind ion CX with atomic H. Currently full quantum mechanical calculations are still sparse due to challenges for computational resource and theory treatment.

On the other hand, experimental techniques have advanced CX to the point where state selectivity can be measured. One of the significant developments is cold target recoil ion momentum Spectroscopy (COLTRIMS; Dörner et al. 2000; Ullrich et al. 2003). By using COLTRIMS, Abdallah et al. (1998) found that measured state-selective capture cross sections of $3d$ to $7l$ agree with coupled-channel calculations for 1 keV u^{-1}, 6.25 keV u^{-1}, and 25 keV u^{-1} Ar^{8+} CX with He. Xu et al. (2021) measured n-resolved capture cross sections for 1 keV/u–25 keV/u Ne $^{(8,9)+}$ CX with He and H_2, and found a good agreement between MCLZ calculations and the measured results for He. Another significant development is high-resolution X-ray spectroscopy. Hell et al. (2016) pointed out that high-resolution measurements of Kα X-ray emission line energies in Si $^{(4-12)+}$ and $S^{(6-14)+}$ can be applied to redetermine the Doppler shifts of from Chandra observations of Vela X-1. Seely et al. (2017) measured the spectra of Ly-series X-ray in O^{8+} CX with Kr, and suggested that autoionizing double capture enhances Ly-α and Ly-β emission lines. However, such X-ray spectrum measurements are sparse.

Here we report a high-resolution measurement of X-ray emissions following CX between Ne^{8+} ions and He and Kr. Kr is a target that can be easily studied in the laboratory and can act as a surrogate for complicated multielectron targets of astrophysical interest. The collision velocities overlap typical solar wind ion velocities and the measured line ratios are compared between He and Kr. The present study allows attention to be drawn regarding the variation of CX-induced

[7] Author is deceased.

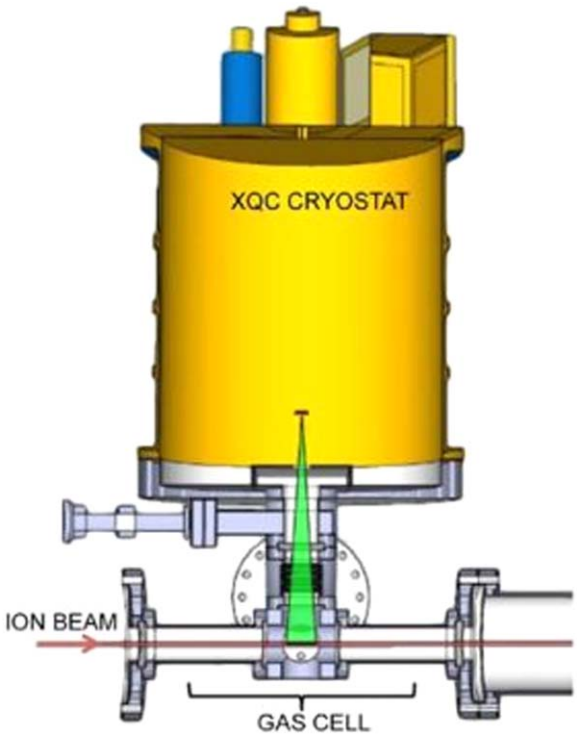

Figure 1. Schematic of the CX cell with the XQC. The viewable portion of the gas cell is shown by the viewing angle from the detector array.

X-ray spectra with different neutrals and collision velocities in modeling astrophysical CX X-ray emissions.

2. Experimental Setup

CX between Ne^{8+} and Kr and He were measured using a beam-gas cell at the Oak Ridge National Laboratory Multicharged Ion Research Facility. The experimental setup is shown in Figure 1 and described elsewhere (Defay et al. 2013; Fogle et al. 2014; Seely et al. 2017). X-ray spectra following CX were recorded by a high-resolution X-ray quantum microcalorimeter (XQC) from the University of Wisconsin and Goddard Space Flight Center (McCammon et al. 2008; Wulf et al. 2019).

Briefly, Ne^{8+} ions from an all-permanent magnet electron cyclotron resonance ion source were first momentum analyzed by a 90° dipole magnet and then accelerated to the collision energies ranging from 800 to 4000 eV u^{-1}, which are corresponding to the solar wind velocity ranging from 392 to 876 km s^{-1}. Several sets of electrostatic deflectors, quadrupole lenses, and adjustable slits were used to optimize the Ne^{8+} ion beam to a few millimeters in diameter. Kr (He) was introduced into a 20 cm long gas cell via a leak valve. The XQC was mounted at 90° with respect to the beam direction. The ions passed through this limited viewing distance in 20–50 ns for the given range of velocities investigated. This allowed the prompt X-ray only due to CX to be registered by the XQC. The XQC has a 6×6 pixel array of HgTe absorbers with each measuring 2.0 mm × 2.0 mm × 0.7 μm in thickness. It was operated at 50 mK and positioned 23 cm above the beam. A set of thin aluminum filters was used to protect XQC from thermal radiation and periodically defrosted.

During the measurement, the beam intensity is approximately 20 nA in the gas cell. The pressure in the gas cell was adjusted in the range $\sim 2 \times 10^{-5}$ Pa and maintained, so that the detector count rate was less than 1 Hz per pixel, which limits pulse pileup. X-ray backgrounds from the ion beam (without gas) and dark counts were periodically measured and found to be insignificant. The net filter efficiencies are shown in Figure 2 for He and Kr CX X-ray measurements.

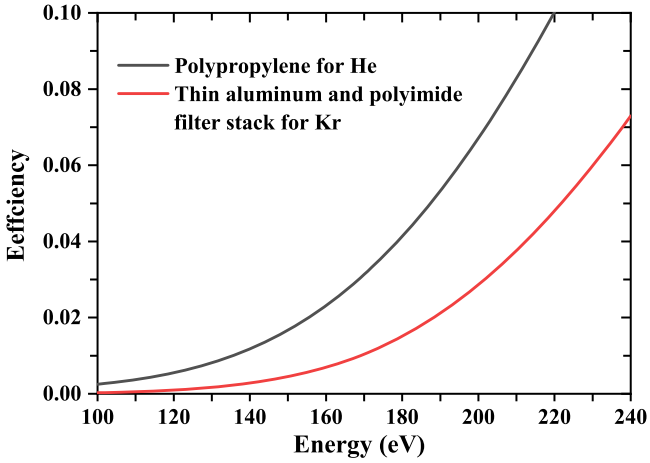

Figure 2 The energy-dependent efficiency of polypropylene and thin aluminum and polyimide filter stack used for X-ray measurements with He and Kr, respectively.

3. Results and Discussion

Figures 3 shows the X-ray spectra measured in Ne^{8+} on He and Kr collisions for the incident velocities of 392, 554, 678, and 876 km s^{-1}, respectively. The spectrum range is from 100 to 240 eV, where the X-ray line energies are calculated from the National Institute of Standard and Technology (Kramida et al. 2020). Gaussian curve fitting was adopted to extract the contributions of each transition. The FWHM of the fitted peaks was constrained to be the same for each spectrum. By iterating the fitting procedure to minimize the χ^2 value of the composite fitting in all spectra, the resulted FWHM is about 7.9 eV. Clearly, for the Ne^{8+} collision with He, the $3d \rightarrow 2p$, $3p \rightarrow 2s$, $4s \rightarrow 2p$, $4d \rightarrow 2p$, $4p \rightarrow 2s$, $5s + 5d \rightarrow 2p$, and $5p \rightarrow 2s$ transitions are identified for the singly excited Ne^{7+} ion after CX. By contrast, additional emission lines of $3s \rightarrow 2p$, $6p \rightarrow 2s$, and $6s \rightarrow 2p$ are observed for Kr as shown in right panel of Figure 3. Note that $5s \rightarrow 2p$ and $5d \rightarrow 2p$ transitions are averaged due to the very small energy difference.

The line ratios are calculated by multiplying the ratios between the Gaussian area of each line and that of $3p \rightarrow 2s$ by the inverse ratios of energy-dependent efficiencies of the filters. The experimentally determined line ratios as a function of collision velocity are shown in Table 1. For the He target, the line ratio for $4p \rightarrow 2s$ is the largest, while the emissions of $5s + 5d \rightarrow 2p$ and $5p \rightarrow 2s$ show minor contributions as well as these emissions from $n = 3$. It can be inferred that $n = 4$ capture is dominant. This quantitatively agrees with a recent state-selective capture measurement, where CX populated $n = 4$ are very selective and the contributions are larger than 96% at present collision velocities (Xu et al. 2021). For the Kr target, the emissions of $5s + 5d \rightarrow 2p$ and $5p \rightarrow 2s$ have large contributions, indicating $n = 5$ capture being dominant. This agrees with the prediction of the scaling law by Janev & Winter (1985) and Otranto et al. (2006) that the dominant capture shifts to a high n level for a small binding energy, which is verified by Xu et al. (2021). For $3d \rightarrow 2p$ emission, the line

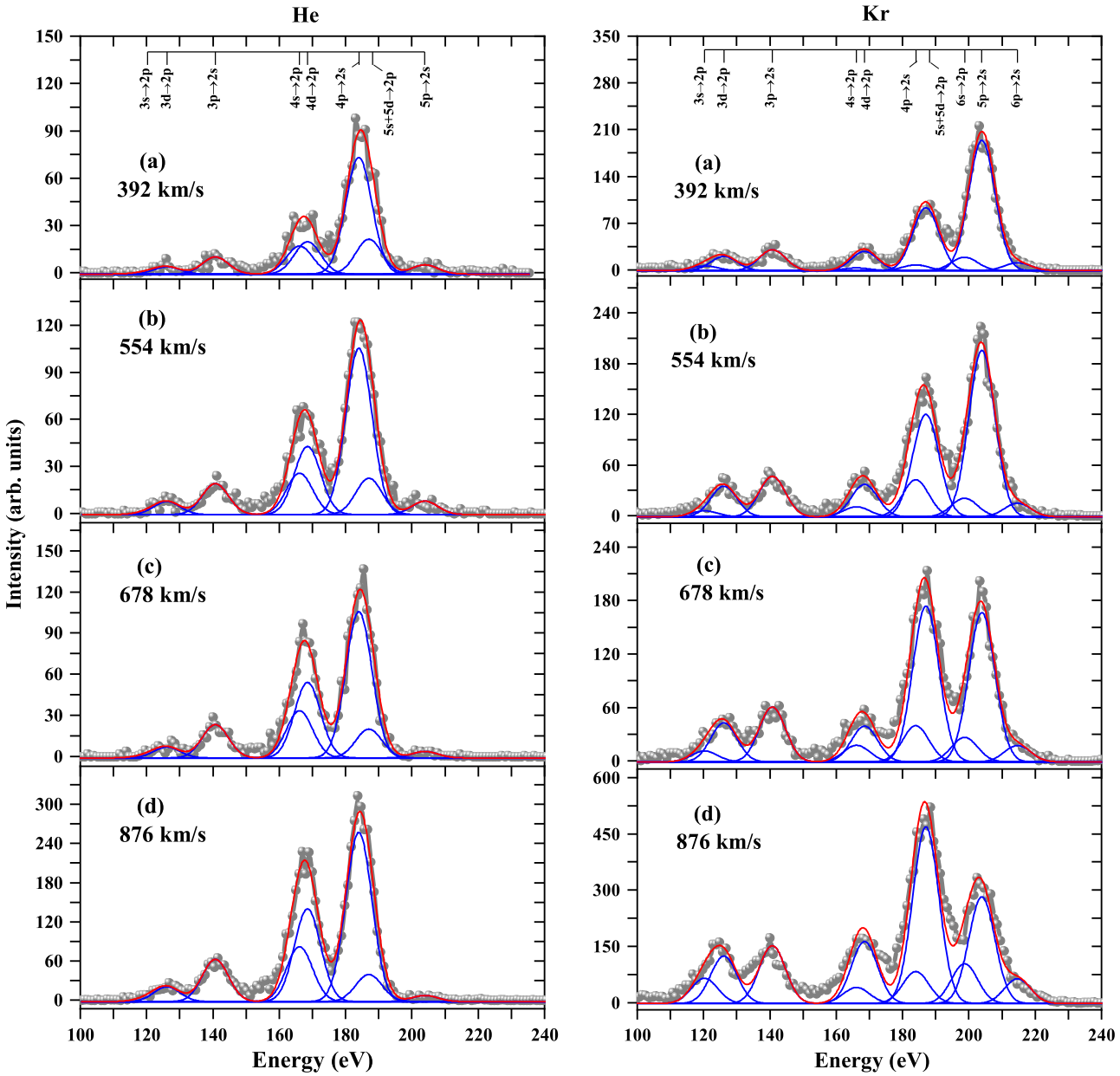

Figure 3. X-ray spectrum from CX between Ne^{8+} and He and Kr. (a), (b), (c), (d) The incident projectile velocities of 392, 554, 678, and 876 km s^{-1}, respectively. Gray spheres, blue lines, and the red line represent the experimental data, Gaussian fitting results, and the sum of Gaussian fitting results, respectively. X-ray spectra for He are also seen in Zhang et al. (2019).

ratios show very weak collision velocity dependence for both He and Kr at present collision velocities. The line ratios of $3d \rightarrow 2p$ for He are smaller than those for Kr, in part because $3d \rightarrow 2p$ emission is being fed by more cascades from higher lying states for Kr than He and because of the possible contribution due to a similar autoionizing double capture (Seely et al. 2017).

Figure 4 shows the CX line ratios associated with He and Kr on a color–color diagram. The line ratios of $4s \rightarrow 2p$ and $4d \rightarrow 2p$ transitions are almost constant for He and larger than those for Kr. By considering the radiative cascade (Politis et al. 1987), we are able to infer that $4s$ and $4d$ state-selective CX cross sections are weakly dependent on the present collision velocities. The decreasing of $4p \rightarrow 2s$ line ratios for He suggests that $4p$ populations decrease with the increase of the collision velocities. The line ratios of $5p \rightarrow 2p$ for the He target are smaller than those for Kr by at least a factor of 7 at the present collision velocities. The latter strongly decreases with increasing velocity. The line ratios of $5s + 5d \rightarrow 2p$ for the He target are smaller than those for Kr by at least a factor of 2. Finally, such line ratio diagrams could facilitate the quantitative diagnostics for the target and velocity-dependent CX processes.

4. Summary

The high-resolution soft X-ray spectra following CX between Ne^{8+} and He and Kr at 392, 554, 678, and 876 km s^{-1} are measured by using the beam-gas technique and high-resolution microcalorimeter X-ray detector. The emission lines of $3s \rightarrow 2p$, $3d \rightarrow 2p$, $3p \rightarrow 2s$, $4s \rightarrow 2p$, $4p \rightarrow 2s$, $4d \rightarrow 2p$, $5s + 5d \rightarrow 2p$, $5p \rightarrow 2s$, and $6p \rightarrow 2s$ are clearly identified, and the line ratios are reported by normalizing each

Table 1
Comparison of the Measured Line Ratios between Ne^{8+} CX with He and Kr

Energy (eV)	Line	Line Ratios for He				Line Ratios for Kr			
		392 km s^{-1}	554 km s^{-1}	678 km s^{-1}	876 km s^{-1}	392 km s^{-1}	554 km s^{-1}	678 km s^{-1}	876 km s^{-1}
120.28	$3s \rightarrow 2p$	...	...	...	...	0.39(0.16)	0.22(0.14)	0.34(0.12)	0.91(0.15)
126.12	$3d \rightarrow 2p$	0.72(0.38)	0.78(0.20)	0.72(0.16)	0.72(0.14)	1.19(0.15)	1.33(0.13)	1.25(0.11)	1.41(0.13)
140.73	$3p \rightarrow 2s$	1	1	1	1	1	1	1	1
166.12	$4s \rightarrow 2p$	0.65(0.16)	0.49(0.07)	0.49(0.07)	0.46(0.05)	0.04(0.06)	0.10(0.05)	0.13(0.05)	0.11(0.05)
168.54	$4d \rightarrow 2p$	0.68(0.16)	0.75(0.08)	0.71(0.07)	0.71(0.06)	0.39(0.06)	0.33(0.05)	0.26(0.04)	0.45(0.06)
184.00	$4p \rightarrow 2s$	1.52(0.26)	1.08(0.09)	0.81(0.06)	0.76(0.05)	0.17(0.03)	0.34(0.03)	0.28(0.02)	0.25(0.03)
187.54	$5s + 5d \rightarrow 2p$	0.33(0.07)	0.18(0.03)	0.11(0.02)	0.10(0.02)	0.73(0.05)	0.60(0.04)	0.64(0.02)	0.73(0.05)
198.70	$6s \rightarrow 2p$	...	...	...	...	0.11(0.02)	0.09(0.02)	0.09(0.01)	0.15(0.02)
203.92	$5p \rightarrow 2s$	0.04(0.02)	0.03(0.01)	0.01(0.01)	0.01(0.01)	1.16(0.07)	0.75(0.04)	0.49(0.02)	0.34(0.02)
214.70	$6p \rightarrow 2s$	...	...	...	...	0.05(0.01)	0.04(0.01)	0.03(0.01)	0.05(0.01)

Note. Errors given in the brackets are statistical errors and determined from the Gaussian fitting of the peak.

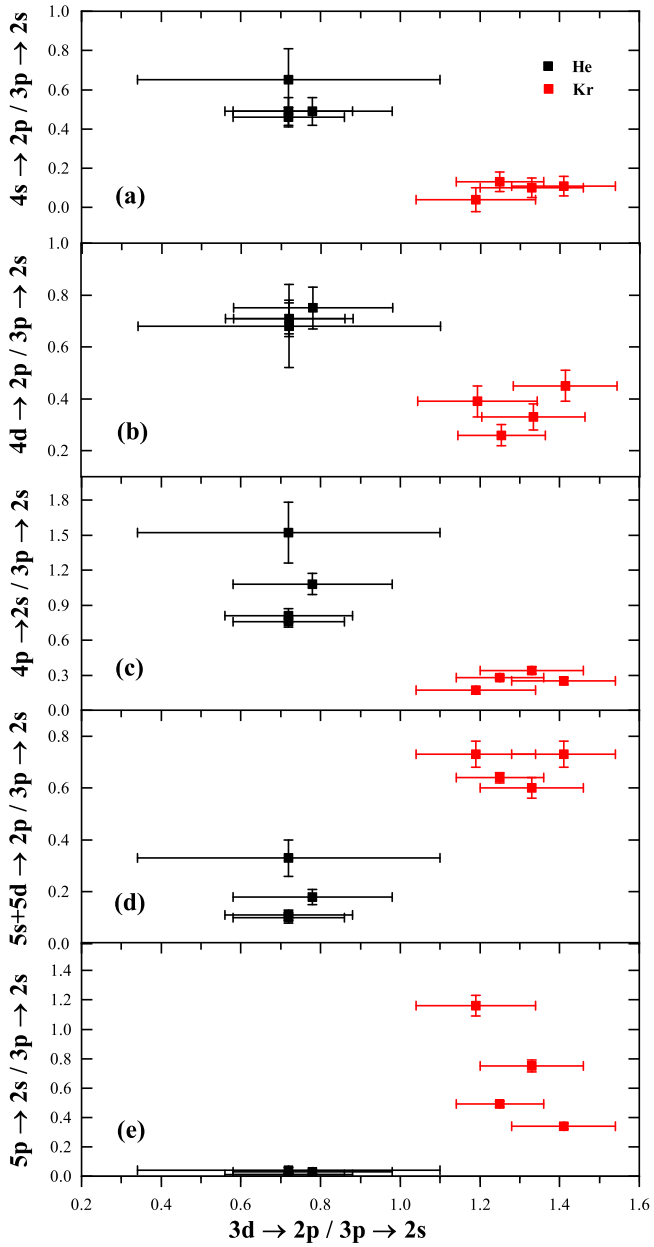

Figure 4. The measured line ratios of CX between Ne^{8+} and He and Kr. Black and red filled squares represent the measured results of He and Kr, respectively.

line intensity to that of $3p \rightarrow 2s$. It is found that the line ratios of $3s \rightarrow 2p$ and $3d \rightarrow 2p$ emissions weakly depend on the collision velocities. The emissions of $4s \rightarrow 2p$, $4p \rightarrow 2s$, and $4d \rightarrow 2p$ for He are dominant over those for Kr. The velocity dependence of these emissions are observed especially for the He target and only the $4d$ line ratio for Kr. However, for the emissions of $5p \rightarrow 2s$ and $5s + 5d \rightarrow 2p$, the emissions from Kr are dominant over those for He and also are velocity dependent. These illustrate the clear target and velocity dependence of CX emissions. Such laboratory measurements of line ratios can be used to accurately determine hot flow velocity and the ambient neutral gas component in astrophysical CX plasma by comparing to the astrophysical observation.

This work was supported by the Strategic Key Research Program of the Chinese Academy of Sciences (XDB340 20000), National Key Research and Development Program of China (grant Nos. 2017YFA0402400 and 2017YFA0402300), and NASA Astrophysics Research and Analysis (APRA) Program NNH18ZDA001N and Solar and Heliosphere Program grant No. NNX13AF31G. R.T.Z acknowledges the hospitality of the physics division at ORNL and thanks Prof. X. Ma for reading the manuscript. This manuscript has been authored by UT-Battelle, LLC under Contract No. DE-AC05-00OR22725 with the U.S. Department of Energy. The United States Government retains and the publisher, by accepting the article for publication, acknowledges that the United States Government retains a nonexclusive, paid-up, irrevocable, worldwide license to publish or reproduce the published form of this manuscript, or allow others to do so, for United States Government purposes. The Department of Energy will provide public access to these results of federally sponsored research in accordance with the DOE Public Access Plan (http://energy.gov/downloads/doe-public-access-plan).

ORCID iDs

R. T. Zhang https://orcid.org/0000-0002-9309-1006
V. M. Andrianarijaona https://orcid.org/0000-0002-1655-9242
F. Jaeckel https://orcid.org/0000-0001-6401-7010
D. Wulf https://orcid.org/0000-0001-7314-9496
K. Morgan https://orcid.org/0000-0002-6597-1030
D. McCammon https://orcid.org/0000-0001-5170-4567
C. C. Havener https://orcid.org/0000-0002-4110-8363

References

Abdallah, M. A., Wolff, W., Wolf, H. E., et al. 1998, PhRvA, 57, 4373
Beiersdorfer, P., Boyce, K. R., Brown, G. V., et al. 2003, Sci, 300, 1558
Bodewits, D., Christian, D. J., Torney, M., et al. 2007, A&A, 469, 1183
Cravens, T. E. 1997, GeoRL, 24, 105
Cravens, T. E. 2000, ApJ, 532, L153
Cravens, T. E. 2002, Sci, 296, 1042
Cumbee, R. S., Henley, D. B., Stancil, P. C., et al. 2014, ApJL, 787, L31
Defay, X., Morgan, K., McCammon, D., et al. 2013, PhRvA, 88, 052702
Dörner, R., Mergel, V., Jagutzki, O., et al. 2000, PhR, 330, 95
Fabian, A. C., Sanders, J. S., Williams, R. J. R., et al. 2011, MNRAS, 417, 172
Fogle, M., Wulf, D., Morgan, K., et al. 2014, PhRvA, 89, 042705
Hell, N., Brown, G. V., Wilms, J., et al. 2016, ApJ, 830, 26
Holmström, M., Barabash, S., & Kallio, E. 2001, GeoRL, 28, 1287
Janev, R. K., & Winter, H. 1985, PhR, 117, 265
Katsuda, S., Tsunemi, H., Mori, K., et al. 2011, ApJ, 730, 24
Kramida, A., Ralchenko, Yu., Reader, J. & NIST ASD Team 2020, National Institute of Standards and Technology, Gaithersburg, MDNIST Atomic Spectra Database (ver. 5.8), doi:10.18434/T4W30F, https://physics.nist.gov/asd
Kuntz, K. D. 2018, A&ARV, 27, 1
Lallement, R. 2004, A&A, 418, 143
Lisse, C. M., Dennerl, K., Englhauser, J., et al. 1996, Sci, 274, 205
Liu, J., Wang, Q. D., & Mao, S. 2012, MNRAS, 420, 3389
McCammon, D., Barger, K., Brandl, D., et al. 2008, JLTP, 151, 715
Mullen, P. D., Cumbee, R. S., Lyons, D., et al. 2017, ApJ, 844, 7
Politis, M. F., Jouin, H., Bonnefoy, M., et al. 1987, JPhB, 20, 2267
Robertson, I. P., Kuntz, K. D., Collier, M. R., Cravens, T. E., & Snowden, S. L. 2009, in AIP Conf. Proc., 1156, The Local Bubble and Beyond II (Melville, NY: AIP), 52
Seely, D. G., Andrianarijaona, V. M., Wulf, D., et al. 2017, PhRvA, 95, 052704
Smith, R. K., Foster, A. R., Edgar, R. J., & Brickhouse, N. S. 2014, ApJ, 787, 77
Otranto, S., Olson, R. E., & Beiersdorfer, P. 2006, PhRvA, 73, 022723
Ullrich, J., Moshammer, R., Dorn, A., et al. 2003, RPPh, 66, 1463
Wulf, D., Eckart, M. E., Galeazzi, M., et al. 2019, ApJ, 884, 120
Xu, J. W., Xu, C. X., Zhang, R. T., et al. 2021, ApJS, 253, 13
Zhang, R. T., Wulf, D., McCammon, D., et al. 2019, in AIP Conf. Proc., 2160 (Melville, NY: AIP), 070004